Journal of Wind Engineering & Industrial Aerodynamics 209 (2021) 104456

Contents lists available at ScienceDirect

Journal of Wind Engineering & Industrial Aerodynamics

journal homepage: www.elsevier.com/locate/jweia

The influence of freestream turbulence on the temporal pressure distribution and lift of an airfoil

Leon Li, R. Jason Hearst *

Department of Energy and Process Engineering, Norwegian University of Science and Technology, Kolbjørn Hejes vei 2, 7034, Trondheim, Norway

ARTICLE INFO

Keywords:
Wind turbine airfoil
Grid turbulence

ABSTRACT

To gain insight on how freestream turbulence (FST) affects the aerodynamics of an airfoil in a systematic manner, the present study investigates a NREL S826 airfoil subjected to seven different incoming flows with varying degrees of FST. The Reynolds number was held at $Re_c = 4.0 \times 10^5$, while the turbulence intensity (T_i) was varied between 0.4% and 5.4%. An increase in T_i increases the maximum lift while having negligible effects on the stall angle. The lift slope in the linear region also generally increased with higher T_i. The latter observation contrasts with some earlier studies, and incoming flow homogeneity is a potential contributing factor to the differences seen here. Periodic pressure fluctuations are seen in the computed lift time-series signal when T_i is between 1% and 2% and the airfoil is operating in the linear region. These fluctuations arise from surface pressure oscillations that are likely excited by the relatively low incoming T_i. The overall effect is a reduction in the time-averaged lift under these operating conditions. At higher T_i, more energetic boundary layers develop over the airfoil's suction side and the effect of these periodic pressure fluctuations is suppressed, leading to an increase in the produced lift.

1. Introduction

Airfoils employed in the field often experience a wide range of incoming flow conditions, especially within the atmospheric boundary layer (ABL); for example, wind turbines in a wind farm or an aircraft on its landing approach. Within the ABL, turbulent flow is inevitable due to the presence of shear, different terrain, and weather systems. In such conditions, the airfoil's flow characteristics can have significant variations. Mücke et al. (2011) conducted a survey at the GROWIAN facility in Germany to measure the atmospheric turbulence intensity between 50 m and 150 m in elevation, and found that the freestream turbulence intensity (T_i) can exceed 40%, with the average being between 5% and 10%. These large variations can have significant impact on the aerodynamic performance of airfoils operating within this environment. Here, $T_i \equiv \langle u'^2 \rangle^{1/2}/U$, where u' is the velocity fluctuations, U is the mean velocity, and $\langle \cdot \rangle$ denotes a time average.

Stack (1931) was one of the first to investigate the effect of freestream turbulence (FST) on the aerodynamic properties of an airfoil by means of a coarse screen mounted in a wind tunnel. The airfoil models were placed at approximately 11.3M downstream of the screen, where M is the mesh length. One of the airfoils tested was a NACA0021 profile, and an increase in T_i caused an increase in the maximum lift and the stall angle, while the lift slope in the linear region remained relatively constant. Similar behaviour was observed for the Clark-Y profile, which is a cambered airfoil with medium thickness, except that the lift slope for the Clark-Y decreased with increasing T_i. In contrast, a NACA0006 airfoil (thin and symmetric) did not exhibit a strong dependence on T_i. This early work highlighted that different airfoils, particularly thin and thick airfoils, respond differently to FST. The subsequent decades saw an explosion in the development of airfoils for a wide range of applications. Some of the studies focused on laminar to turbulent transition in the airfoil boundary layer, such as the early works of Owen and Klanfer (1953) and Gaster (1967). This is important for the development of airfoils for low speed, subsonic applications, where a significant portion of the boundary layer over the airfoil surface could be laminar. Mueller et al. (1983) highlighted the sensitivity of airfoil performance to Reynolds number, airfoil surface finish, and FST. They stressed the need for future investigations to carefully isolate the effect of each of these factors that influences the aerodynamics of an airfoil. Hoffmann (1991) tested a NACA0015 airfoil subjected to five different incoming turbulent flows ranging from 0.25% to 12% in T_i created by a set of rods. The airfoil was placed at $x/M = 7.6$ for the highest T_i case. There was a marked increased in the maximum lift and the stall angle when T_i increased from 0.25% to 9%. Furthermore, the maximum lift coefficient (C_l) showed a linear trend

* Corresponding author.
E-mail addresses: leon.li@ntnu.no (L. Li), jason.hearst@ntnu.no (R.J. Hearst).

https://doi.org/10.1016/j.jweia.2020.104456
Received 19 June 2020; Received in revised form 30 October 2020; Accepted 21 November 2020
Available online xxxx

with respect to T_i up to 9%, after which it plateaued. Here $C_l = \frac{L'}{\frac{1}{2}\rho_\infty U_\infty^2 c}$, where L' is the sectional lift force per unit span, ρ_∞ is the freestream fluid density, U_∞ is the freestream velocity, and c is the chord length of the airfoil. Swalwell et al. (2001) investigated a NACA0021 profile subjected to three different T_i at 0.6%, 4%, and 7% at a chord Reynolds number $Re_c \approx 3.5 \times 10^5$. The lift slope did not change significantly, but the stall angle increased with increasing T_i. Butler et al. (2001) studied the effect of different integral length scales on the heat transfer of an array of low-pressure gas turbine blades. It was found that the pressure distribution, Reynolds number, and turbulence intensities had a higher impact on the location of the suction-side boundary layer transition than integral length scale. Although this was primarily a study on heat transfer, it still gave some insights into the aerodynamic behaviour of a highly cambered airfoil exposed to elevated FST. As T_i increases, the transition point moves upstream, and thus more of the airfoil is covered by a turbulent boundary layer, which is more resistant to flow separation. Another experimental study for gas turbine airfoils was done by Michálek et al. (2012) on a T106C low-pressure turbine blade with up to $T_i = 3.2\%$. The overall effect of elevated T_i is that it promotes boundary layer reattachment, consistent with the observations made by Butler et al. (2001). The effect is, however, diminished at higher Reynolds numbers on the order of 10^5. At the lower end of turbulence intensity levels, Huang and Lee (1999) focused on the effect of FST between 0.2% and 0.65% on a NACA0012 profile. It was observed that even for $T_i < 1\%$, FST has a marked positive effect on the maximum lift and stall angle. Wang et al. (2014) extended T_i to 6%, also for a NACA0012 profile, and found a similar increase in the maximum lift at $Re_c = 2.0 \times 10^4$, with no significant variations in the stall angle. Furthermore, the lift slope did not change significantly even at $T_i = 6\%$. It should be noted here that both studies on the NACA0012 profile had Re_c on the order of 10^3 to 10^5, with no clear evidence that the behaviour observed were Reynolds number independent. Ravi et al. (2012a) investigated the lift of a thin flat-plate with an elliptical leading edge and tapered trailing edge subjected to T_i from 1.2% to 12.6%, and found that the lift slope decreased with increasing T_i, while the stall angle increased. The airfoil model for the most turbulent case was placed around $x/M = 13$ downstream of the passive turbulence grid. The differences observed for the lift slope behaviour by Wang et al. (2014) and Ravi et al. (2012a) again highlight the different behaviour of thick and thin airfoils.

Focusing on wind turbine applications, Devinant et al. (2002) observed that the maximum lift and the stall angle of a NACA 65_4-421 airfoil increased with higher T_i, but the lift slope decreased. This is similar to the trend observed by Ravi et al. (2012a) even though the two airfoils investigated are drastically different (thin flat plate for micro aerial vehicles compared to thick cambered airfoils for wind turbines). The FST was generated through passive grids, the largest of which was able to achieve a T_i of 15.4%. Although in this configuration, the airfoil model was placed at $x/M = 5$. At this location, grid generated turbulent flows show significant inhomogeneity in their mean velocity profiles (Ertunç et al., 2010; Hearst and Lavoie, 2014; Isaza et al., 2014). The observed decrease in lift slope with increasing T_i is somewhat contrary to the observations of Wang et al. (2014), as well as with those by Schneemann et al. (2010), who also reported that the lift slope showed no significant change with increasing T_i for a Wortmann FX79-W-151A wind turbine airfoil. Furthermore, Wang et al. (2014) found the effects of FST on their lift curve to be limited to near stall, as only $C_{l,\max}$ increased while both the lift slope and stall angle remained relatively constant. Cao et al. (2011) tested a Selig S1223 airfoil with turbulence intensities of 4.1% and 9.5%. The airfoil was originally developed for high-lift low Reynolds number applications, but in their study it is considered as a candidate for vertical axis wind turbines. The stall characteristics are much smoother in the more turbulent case, and this was observed for Reynolds numbers from 5.5×10^4 to 1.0×10^5. Contrary to other studies, there were no significant improvements in either the maximum lift or the stall angle with increasing T_i. Kamada et al. (2011) tested a DU93-W-210 wind turbine airfoil for two flow conditions, T_i at 0.15% and 11%. The trend observed is similar to Devinant et al. (2002) in that the maximum lift increased and the lift slope decreased with elevated T_i. A passive grid was used in this study and the model was placed at about $x/M = 6.6$ downstream. Maldonado et al. (2015) used an active grid to generate T_i of 6.14% for the testing of a NREL S809 wind turbine airfoil. The model was placed at $x/M \approx 39$ downstream of the grid, and an overall improvement in its aerodynamic properties was observed. Both the lift slope and the maximum lift increased, while the stall angle remained the same. The pressure suction peak was also higher for every angle of attack (α) except 0°. Particle image velocimetry (PIV) analysis showed that at $\alpha = 16°$, the flow separation point is farther downstream on the suction side with higher T_i. Li et al. (2016) tested a self-developed wind turbine airfoil and found that the maximum lift increased with higher T_i, with no significant change to the lift slope in the linear region. The study covered T_i up to 13.9% and Reynolds numbers up to 2.0×10^5. Turbulence was generated by a set of four passive grids, the largest of which was placed $x/M = 7$ upstream of the model. Recently, Sarlak et al. (2018), studying a NREL S826 airfoil, found that an increase in T_i up to 2% gave a significant improvement in the lift performance at $Re_c = 4.0 \times 10^4$, but it offered no visible improvement at $Re_c = 1.0 \times 10^5$. In this case, FST was generated by sets of three wires of different diameters placed 5.5c upstream of the airfoil, not by a turbulence grid that covers the entire cross-section of the test-section. As as result, the FST generated by Sarlak et al. (2018) is not homogeneous across the test section. However, the study's main focus was on the dynamic stall behaviour of this airfoil, not on the effect of FST, and has yielded some interesting results that will be discussed later in this section.

Table 1 summarizes the details from selected previous investigations. The numerous studies investigating the effect of FST on airfoil aerodynamics sometimes produce contradictory results. Some reported that the lift slope decreased while the maximum lift increased with increasing FST (Devinant et al., 2002; Ravi et al., 2012a; Kamada et al., 2011), others reported an increase in both the lift slope and the maximum lift (Maldonado et al., 2015), while still others reported no changes to the lift slope (Wang et al., 2014; Schneemann et al., 2010; Li et al., 2016). It would appear that most disagreements are on the behaviour of the lift slope as FST increases. This can be attributed to several factors, including different airfoil profiles, Reynolds number dependency, and incoming flow conditions. The present study seeks to address these three issues. The airfoil profile used for this investigation is the NREL S826 wind turbine airfoil. Originally published by Somers (2005) from the National Renewable Energy Laboratory in the USA, it was designed for horizontal-axis wind turbines with rotor diameters between 20 m and 40 m. This airfoil has already been used in several experimental and numerical studies as a generic reference wind turbine airfoil (e.g., Sarmast and Mikkelsen, 2012; Sarlak et al., 2014; Sarlak and Sørensen, 2018; Sarlak et al., 2018; Yalçın et al., 2018; Bartl et al., 2019; Hann et al., 2020), and the present study seeks to contribute to the growing body of data available. There are some complex flow phenomena for this airfoil at low to moderate Reynolds numbers (4.0×10^4 to 2.0×10^5), such as a stall hysteresis loop and 3-D stall cells. Interestingly, the stall cells are more prominent at $Re_c = 1.0 \times 10^5$ and 2.0×10^5 than at lower Re_c (Sarlak et al., 2018; Sarlak and Sørensen, 2018). Nevertheless, one of the objectives of this study is to remove Reynolds number dependence as a potential factor that influences the aerodynamic characteristics of this airfoil. As the goal is to focus only on the effect of FST on pressure and lift behaviour, it is desirable that the Reynolds number be kept as high as possible. The design Reynolds number of this airfoil is $\sim 1.5 \times 10^6$. While this was not achievable with our present experimental facility, the experiments were conducted at a sufficiently high Reynolds number to remove any Reynolds number dependence, as will be shown in later sections. Thus, the results obtained are representative of the field behaviour of this airfoil.

The incoming flow homogeneity is another potential factor contributing to the observed differences in lift slope behaviour. As stated earlier,

Table 1
Summary of selected previous studies on the effect of FST on airfoil aerodynamics; ↑ denotes increase, ↓ denotes decrease, and ≈ denotes constant. Missing information are denoted by ·. The experimental parameters of the present study are also listed for comparison purposes. x/M^* is the position of the airfoil relative to the turbulence generating grid for the highest T_i case only. x/M for Sarlak et al. (2018) is not applicable as they used sets of three wires instead of a space-filling turbulence grid.

Study	Geometry	Application	Re_c [$\times 10^3$]	T_i [%]	x/M^*	$C_{l,\max}$	As FST increases, Stall α	Lift slope
	USA 35-A	·				↓	·	·
	USN PS6	·				↓	·	·
Stack (1931)	Clark-Y	General	52–3400	·	11.3	↑	↑	↓
	NACA0006	General				≈	·	·
	NACA0021	General				↑	↑	≈
Swalwell et al. (2001)	NACA0021	General	350	0.6–7	·	↑	↑	≈
Huang and Lee (1999)	NACA0012	General	82–173	0.2–0.7	·	↑	↑	≈
Wang et al. (2014)	NACA0012	General	5.3–20	0.6–6	14	↑	≈	≈
Hoffmann (1991)	NACA0015	General	250	0.25–12	7.6	↑	↑	≈
Cao et al. (2011)	S1223	Low *Re*	55–100	4.1–9.5	12.4	≈	≈	≈
Ravi et al. (2012a)	Thin flat plate	Low *Re*	75	1.2–12.6	13	↑	↑	↓
Devinant et al. (2002)	NACA 65_4-421	Wind turbine	100–700	0.5–15.4	5	↑	↑	↓
Schneemann et al. (2010)	FX79-W-151A	Wind turbine	700	$<1-6.7$	·	↑	↑	≈
Kamada et al. (2011)	DU93-W-210	Wind turbine	350	0.5, 11	6.6	↑	↑	↓
Maldonado et al. (2015)	NREL S809	Wind turbine	208	6.14	39	↑	≈	↑
Li et al. (2016)	Self-developed	Wind turbine	50–200	0.15–13.9	7	↑	↑	≈
Sarlak et al. (2018)	NREL S826	Wind turbine	40	0.1–1.9	N/A	↑	≈	↑
			100	0.2–1.7	N/A	≈	≈	≈
Present study	NREL S826	Wind turbine	400	0.4–5.4	16.1	↑	≈	↑

flow conditions at $x/M < 10$ show significant inhomogeneity in both the mean velocity and the velocity fluctuation profiles (Ertunç et al., 2010; Hearst and Lavoie, 2014; Isaza et al., 2014). Typically for grid turbulence, approximately homogeneous isotropic turbulence is achieved at around $x/M = 30$ (e.g., Comte-Bellot and Corrsin, 1966). This is important for experimental aerodynamics for airfoils as the forces are typically either directly measured or integrated from pressure distributions. The latter is especially sensitive to flow inhomogeneity as it only computes the sectional lift at one span location, and if the flow is inhomogeneous, it follows that the computed forces are highly dependent on the spanwise location of the measurement plane. Direct force measurements give the averaged forces across the entire measured span, thus integrating the inhomogeneous effects. It follows that the results would vary depending on the degree of flow inhomogeneity. In addition, it has been documented that at high α, airfoils can develop 3-D stall structures on the surface near stall (Sarlak et al., 2018; Sarlak and Sørensen, 2018). Any non-uniformity in the incoming flow is likely to interact with these 3-D structures and cause unintentional effects. Thus, in order to isolate the effect of FST on the aerodynamic behaviour of an airfoil, particularly near stall, the incoming flow needs to be as homogeneous as possible. There is evidence in previous studies that flow inhomogeneity has a general effect on airfoil aerodynamics. The investigations of Devinant et al. (2002) and Kamada et al. (2011) were performed at $x/M = 5$ and 6.6, respectively, and both reported a decrease in the lift slope with increasing T_i. In contrast, Maldonado et al. (2015) performed their experiments at $x/M = 39$, within the homogeneous flow region, and reported the opposite behaviour. All three investigations performed tests at $\sim 5\%$ turbulence intensity on wind turbine airfoils.

The present investigation incorporates combinations of passive turbulence grids to generate seven different T_i, the largest of which has the airfoil model located at a similar mesh lengths distance as Wang et al. (2014), who reported a root mean squared velocity profile variation of less than 0.9%. Additionally, the T_i achieved in the present study are representative of the flow conditions seen in the field. Given that modern wind turbines often have tip speed ratios (TSRs) between 6 and 8 for maximum power efficiency (Bianchi et al., 2007), and the largest wind gusts can exceed 40% (Mücke et al., 2011), it follows that the actual T_i experienced by the majority of the blade is below 10%. This is especially true for the S826 airfoil, which is primarily intended to be used at the tip section of the blade, corresponding to the 0.95 blade radial position. A typical atmospheric T_i of 10% would correspond to a T_i of 1.7% as experienced by the rotor tips, assuming a TSR of 6. The T_i range chosen for this study, the highest of which is 5.4%, thus covers the expected field flow conditions for this airfoil. We would like to note that although the T_i values of the present study match those found in field, we cannot match the scales of turbulent eddies found in typical ABLs, which can exceed the turbine size.

Lastly, we seek to combine the spectral analyses of the pressure and lift coefficients with their time-averaged counterparts. Spectral analysis of the lift coefficients has been done by Blackburn and Melbourne (1996) and Sicot et al. (2006) on a cylinder and an airfoil respectively, while Ravi et al. (2012b) and Watkins et al. (2010) performed spectral analysis on the pressure distributions. Sarlak et al. (2018) analyzed the surface pressure fluctuations of the NREL S826 airfoil, but stopped short of examining the frequency content of the fluctuations. There has been very few studies to date that focus on the temporal analysis of pressure on an airfoil surface. To the authors' knowledge, this is the first attempt at combining the spectral analyses of both the lift and pressure signals with their time-averaged counterparts for a study on the aerodynamics of an airfoil subjected to different turbulent incoming flows.

2. Experimental equipment and procedure

The experiment was performed in the large closed-loop wind tunnel at the Norwegian University of Science and Technology. The test section has a rectangular cross section measuring 1.85 m × 2.71 m, and its length is 11.15 m. The wind tunnel is driven by a 220 kW fan controlled via a variable frequency drive. The fan is located downstream of the test section. The roof panels of the test section are adjustable to achieve an approximately zero-pressure gradient potential core in the test section. The maximum speed achievable is around 23 m/s. The wind tunnel is instrumented with a Pitot-static tube near the inlet of the test section and a thermocouple for temperature measurements. The dynamic pressure and test section ambient temperature were measured for each α for all the test cases. The ambient atmospheric pressure was measured at the beginning and end of each test case with a mercury barometer.

The airfoil was manufactured from synthetic polyurethane blocks through CNC-machining. The surface is sanded and painted to be aerodynamically smooth. For more information about the airfoil model's design and manufacturing process, see Bartl et al. (2019). The model is

mounted vertically in the test section and secured to a turntable in the floor. No end plates were used because the airfoil extends from the floor to the ceiling and the boundary layer effects have been shown to be negligible in the centre 2/3 of the span (Bartl et al., 2019). Regardless, the sectional pressure measurements do not integrate the loads across the entire airfoil, but only represent the loads in the measurement plane. The leading edge of the airfoil is located 3.85 m, or 8.56c from the inlet of the test section, where $c = 0.45$ m is the chord length of the airfoil. This was fixed due to the mounting mechanism of the model to the turntable. A schematic drawing of the setup can be found in Fig. 1. At the mid-span of the airfoil, there are 32 pressure taps distributed around the circumference, with 19 taps on the suction side and 13 taps on the pressure side. The locations of the pressure taps are shown in Fig. 2. The pressure taps are connected to a Scanivalve MPS4264 miniature pressure scanner mounted inside the model, which can sample all 32 ports simultaneously. The turntable enables α to be changed from -8° to $+18^\circ$, covering the operating, stall, and post-stall regions of the airfoil. The maximum blockage ratio of the model is estimated to be about 5.6%. Blockage correction was not applied as this is within the range where such corrections can be avoided (West and Apelt, 1982). Indeed, the freestream velocity is only increased by less than 0.2% according to the solid blockage correction estimated from Barlow et al. (1999), which is within the measurement accuracy of the present set-up. At each α, the pressure distribution data was measured with the scanner at 800 Hz for 60 s. The pressure time-series signals were digitally filtered with a 7th-order low-pass Butterworth filter at a cutoff frequency $f_c = 140$ Hz in order to remove the frequency content associated with the noise floor. The sampling frequency of 800 Hz is well above the required Nyquist frequency for this cutoff. It should be noted here that 140 Hz represents the frequency response limitation of the setup, and not the frequency bound of the underlying physics. The freestream velocity U_∞ was set to 14.5 m/s, for a chord Reynolds number $Re_c = 4.0 \times 10^5$.

Additional tests were carried out for $Re_c = 2.0 \times 10^5$, 3.0×10^5, and 4.4×10^5 for different freestream turbulence levels ranging from <1% to 4% to check for Reynolds number invariance of the lift and pressure characteristics. Fig. 3 shows the lift coefficients for $T_i = 0.40\%$ and 3.93%. It can be seen that the lift curves for $Re_c = 4.0 \times 10^5$ and 4.4×10^5 collapse with each other for both cases, and thus the behaviour of the airfoil is effectively Reynolds number independent at the primary test Re_c. We chose to test this airfoil at this Re_c because we want to remove Reynolds number dependence as a potential factor that influences the aerodynamic behaviour assessed in the present experiments. Numerous previous studies have demonstrated the Reynolds number dependence of this airfoil at low to moderate Reynolds numbers of around 10^5, and our test Re_c avoids this flow regime. Bartl et al. (2019) also found the lift characteristics of this airfoil to be relatively Reynolds number independent for $Re_c \geq 4.0 \times 10^5$. We note that this is still an order of magnitude below the intended operating conditions for this airfoil, $Re_c \approx 1.5 \times 10^6$ (Somers, 2005), but is in the highest range of achievable Re_c in this experimental facility and roughly Re_c-independent for this range of Reynolds numbers.

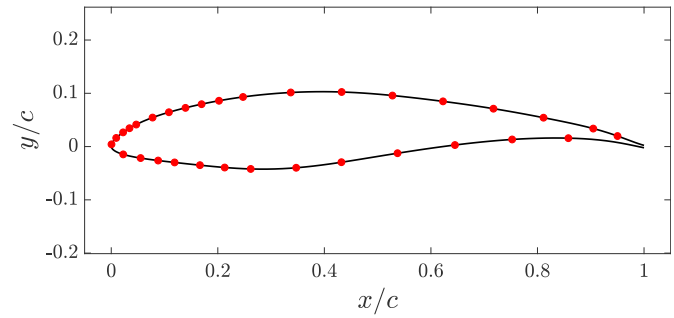

Fig. 2. Airfoil cross section with pressure port locations marked in solid red circles. (For interpretation of the references to colour in this figure legend, the reader is referred to the Web version of this article.)

To generate the turbulent freestream flows, four different passive grids were used in combination to create a total of seven different flow cases, including a quasi-laminar reference case denoted as REF. The freestream turbulence intensity, T_i, for REF measured at the leading edge of the airfoil is around 0.40%. This flow was achieved by mounting a fine steel mesh, which is one of the grids used, at the test section inlet. The other different flow conditions were made by having two locations for inserting the grids. The first one is placed at the inlet of the test section, and the second location is 2.57 m downstream. The physical properties of the four grids are listed in Table 2. The seven different incoming flows and their homogeneity and turbulence statistics are provided in Table 3. For the two-grid configurations, the normalized airfoil leading edge location, x/M, is measured from the second grid and uses the mesh size of the second grid. Due to the limitation of the setup, the location of the airfoil model was fixed with respect to the wind tunnel, and its position relative to the grids varies with different grid configurations. The naming convention given to the six turbulent flow cases contains the T_i values measured at the leading edge of the airfoil at mid-span, rounded to the first decimal place. For the most turbulent case FST5.4, the airfoil was located 16.1M downstream of the aft grid. The root mean squared (RMS) variation in U for this flow case is $I_U/U\ (y) = 0.88\%$ as shown in Table 3, where $I_U = \left(\frac{1}{N-1}\sum\left(U(y_i) - \overline{U(y)}\right)^2\right)^{\frac{1}{2}}$ is the standard deviation of the velocity profile, and $U\ (y)$ is the averaged value of the spanwise velocity profile. While 16.1M is less than the 30M usually found in the literature for homogeneous isotropic grid turbulence, it is still much farther downstream than the set-up in Devinant et al. (2002), and is similar to Wang et al. (2014), who reported $I_U/U < 0.9\%$ at 14M.

The turbulence statistics were measured with a Dantec 55P11 single hot-wire probe. It has a tungsten sensing element measuring 1.25 mm in

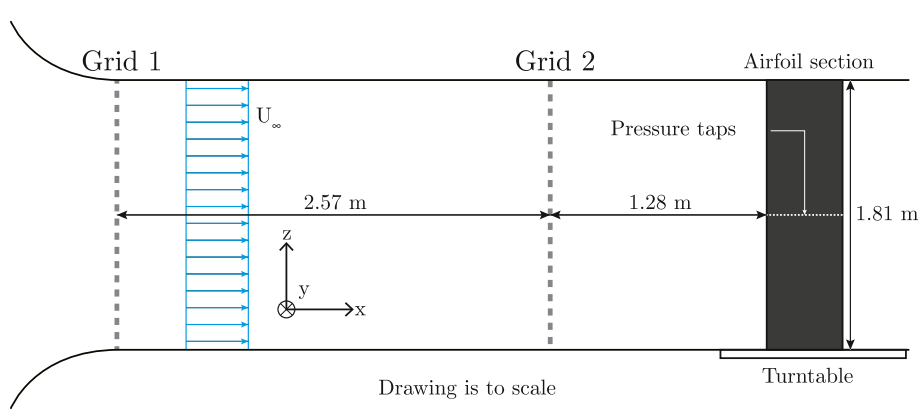

Fig. 1. Schematic of the experimental setup.

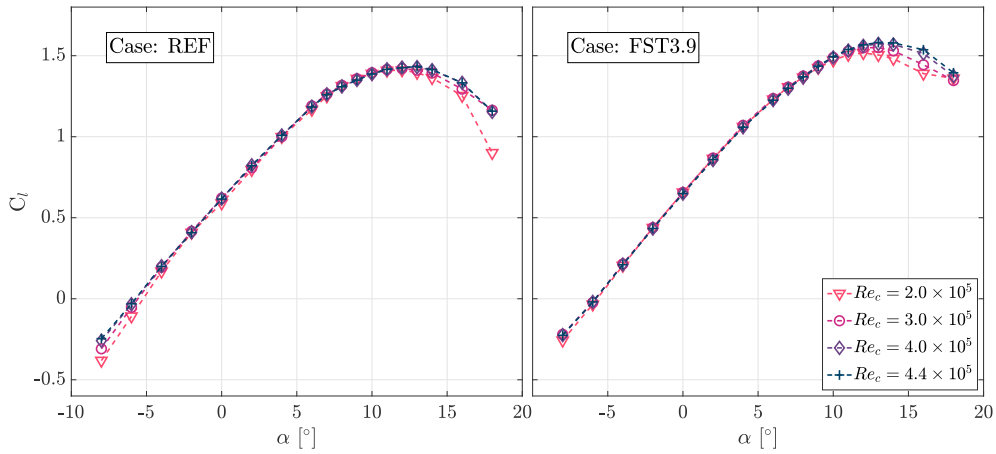

Fig. 3. Lift coefficient for REF and FST3.9 for multiple Reynolds numbers.

Table 2
Summary of the grid physical properties.

Grid	Description	Mesh length, M	Solidity, σ
SG1	Mono-planar steel square mesh	3.00 mm	0.33
SG2	Mono-planar steel square grid	40.0 mm	0.44
WG1	Bi-planar wooden square grid	123 mm	0.33
WG2	Bi-planar wooden square grid	240 mm	0.35

Table 3
Summary of the flow homogeneity and turbulence properties of the incoming flows. The turbulence properties are taken at the leading edge of the airfoil, at mid-span. x/M is measured from the farthest downstream grid (when there is one grid, it is Grid 1; when there are two grids, it is Grid 2).

Case	Grid 1	Grid 2	x/M	I_U/U (y) [%]	u'/U [%]	L_{ux}/c
REF	SG1	–	1638	0.43	0.40	–
FST1.1	SG2	SG1	546	0.44	1.13	0.067
FST1.6	SG2	–	96.4	0.58	1.61	0.073
FST2.1	WG1	SG1	546	0.25	2.14	0.100
FST3.0	WG1	–	31.3	0.58	3.00	0.131
FST3.9	WG2	SG1	546	0.42	3.93	0.156
FST5.4	WG2	–	16.1	0.88	5.39	0.227

length and 5 μm in diameter. The probe was operated at an overheat ratio of 1.8, and was controlled via a Dantec StreamLine Pro anemometer. To measure the turbulence statistics at the leading edge of the airfoil, the probe was secured to a rigid metal stand that was fastened to the test section floor. Homogeneity scans were carried out by mounting the probe via a sting to a traverse system with three degrees of freedom. To avoid mechanical vibrations of the hot-wire holder, the homogeneity scans were performed at a lower Reynolds number of 3.0×10^5. This is, however, still representative of the flow homogeneity at the test chord Reynolds number of 4.0×10^5 since homogeneity in grid turbulence is largely Reynolds number independent (e.g., Larssen and Devenport, 2011). The scan consists of 17 equally spaced measurement points spanning $-1.6 \leq y/c \leq +1.6$. The overall uncertainty in the measured turbulence intensity is estimated to be on the order of 1% according to the method of Benedict and Gould (1996). Standard Reynolds decomposition is used to separate the velocity $u(y)$ into a time-averaged component $U(y)$ and a fluctuating component $u'(y)$, namely $u(y) = U(y) + u'(y)$. Fig. 4 shows the flow homogeneity profiles of the normalized freestream velocity $U(y)/U_0$, velocity fluctuation $u'(y)/U(y)$, and integral length scale $L_{ux}(y)/c$ for all the cases. U_0 is the average of $U(y)$ for each case.

3. Mean pressure distributions and lift coefficients

The time-averaged pressure measurements were computed for each pressure port location. The same technique as used by Bartl et al. (2019) was used here to close and integrate the normalized pressure distribution $C_p = \frac{P-P_\infty}{\frac{1}{2}\rho_\infty U_\infty^2}$, where P is the local surface pressure and P_∞ is the freestream static pressure. Fig. 5 shows the C_p distributions for all test cases at selected α. The angles shown are the zero-lift angle ($\alpha \approx -6°$), the zero angle, linear region angles ($\alpha = 6°, 10°$), the stall angle ($\alpha = 13°$), and a post-stall angle ($\alpha = 18°$). The REF measurements presented herein are in good agreement with previous measurements on the same model in the same facility using different equipment (Bartl et al., 2019). For the turbulent cases, it can be observed that within the linear range ($-6° \leq \alpha \leq 7°$), cases with higher FST exhibit more negative C_p values around the suction peak, which implies that more lift is generated for these cases. At

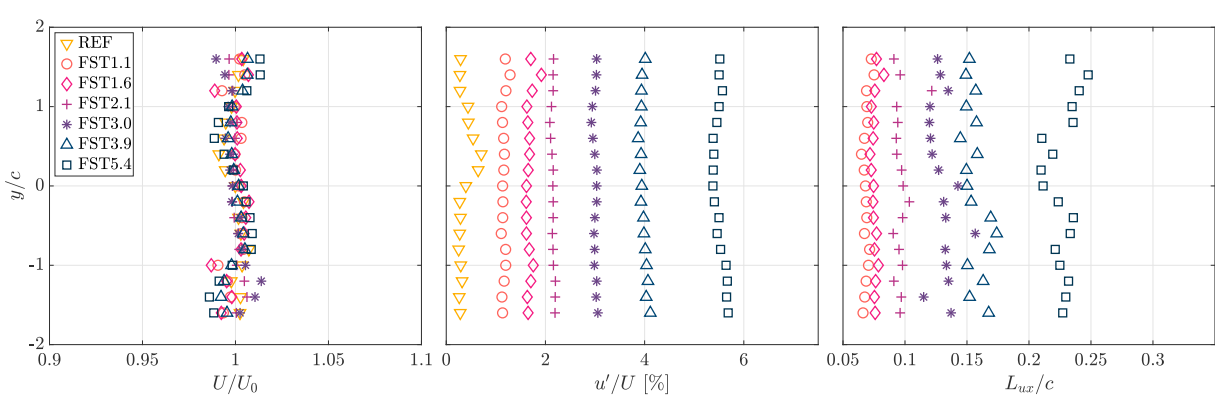

Fig. 4. Flow homogeneity profiles for all test cases for U/U_0, u'/U [%], and L_{ux}/c.

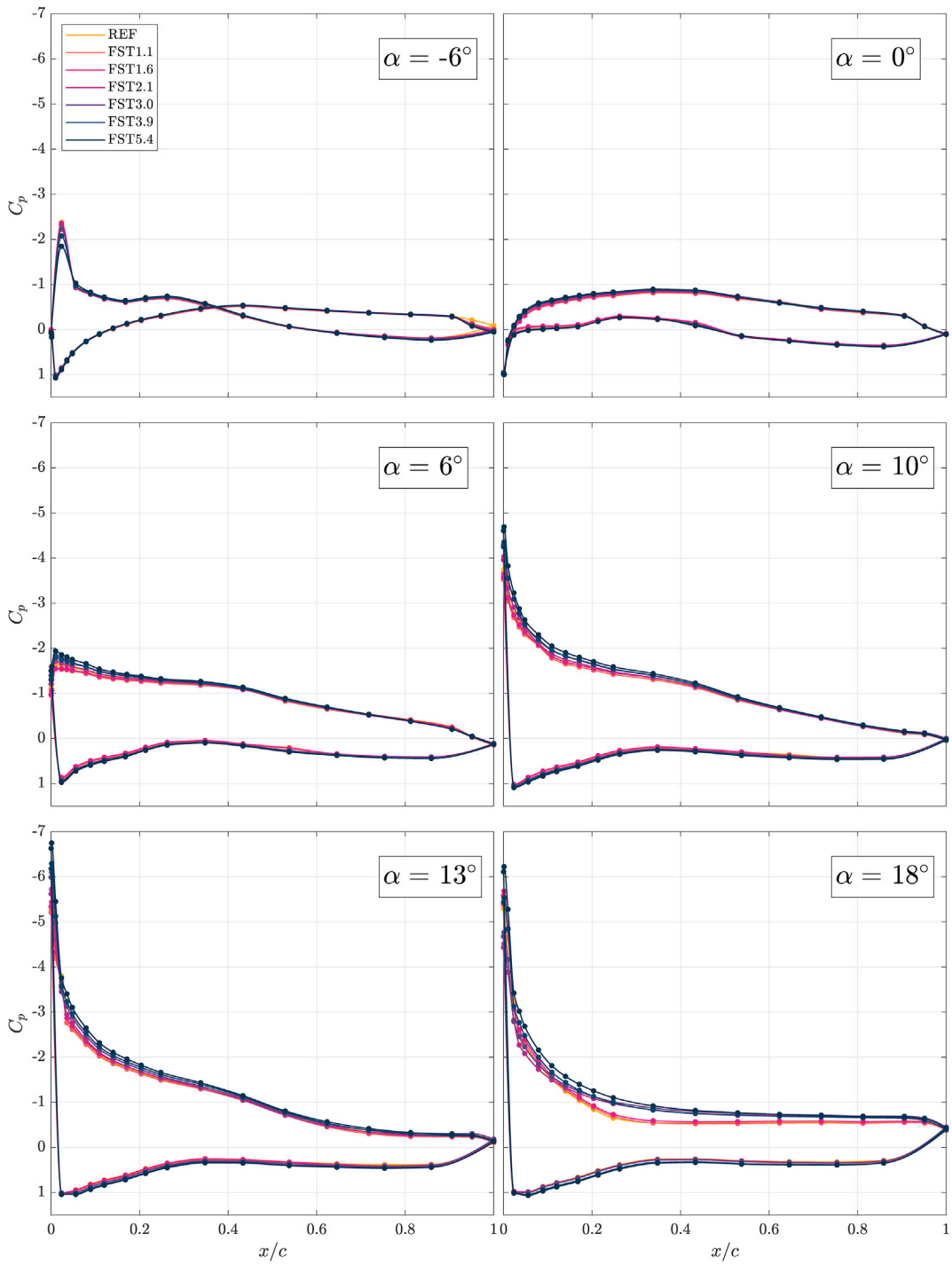

Fig. 5. Pressure coefficient C_p for all cases at selected α.

the highest α, there is a distinct grouping of the C_p distribution on the suction side for $x/c > 0.1$. Cases where $T_i > 2\%$ show a gentler pressure recovery and more negative values than cases with $T_i < 2\%$. Flow separation on the airfoil surface causes a region with relatively constant low pressure, and this manifests as plateaus in the suction side C_p distribution. The start of the plateaus marks the start of the separated flows. The C_p distributions at $\alpha = 18°$ show a delayed onset of the plateau region for $T_i > 2\%$. This suggests that flow separation in the post-stall region under elevated FST is delayed.

Fig. 6 shows the C_l vs. α relation for all test cases calculated from integrating the C_p distributions. The pressure drag can be similarly calculated, however, it is just one, relatively small, constituent part of the total drag and thus we primarily focus on the lift in the present work. Both the maximum lift and the lift slope in the linear region generally increase with T_i, while C_l for $\alpha \leq -4°$ remains relatively unaffected by FST. The zero-lift angle remains constant at $-6°$ for all cases and appears to be the point where the C_l curves "fan out" as FST increases. This behaviour is consistent with the observations of previous studies such as Devinant et al. (2002) and Wang et al. (2014). Fig. 7 shows the extracted maximum lift coefficient from each case, and it can be seen that $C_{l,\,\max}$ is relatively constant from REF to $T_i = 1.1\%$, then it increases in a linear fashion with respect to T_i. This is consistent with the observations of Devinant et al. (2002) and Wang et al. (2014). The stall angle where $C_{l,\,\max}$ is reached appears unaffected by turbulence intensity, as it remains

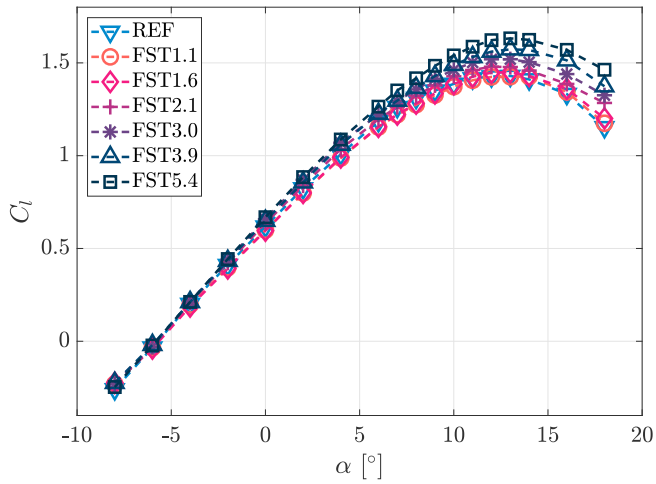

Fig. 6. Lift coefficient C_l for all test cases at $Re_c = 4.0 \times 10^5$.

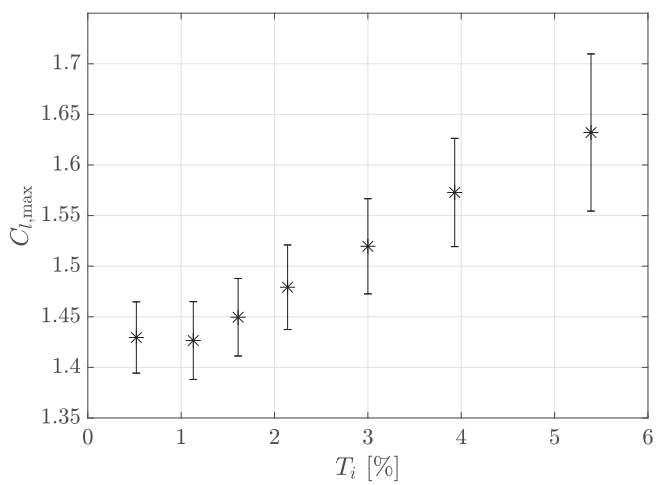

Fig. 7. $C_{l,\max}$ at the stall angle for all test cases; marker sizes are representative of the uncertainty for T_i.

relatively constant at $\alpha = 13°$, as can be seen in Fig. 6. This contrasts with the results of Devinant et al. (2002) and Kamada et al. (2011), where the stall angle increased with FST. However, the constant stall angle behaviour agrees with the observations of Wang et al. (2014) and Maldonado et al. (2015). It is possible that flow homogeneity plays a role in the behaviour of stall angles here, as Wang et al. (2014) and Maldonado et al. (2015) conducted their experiments farther downstream of their grids ($x/M = 14$ and 39, respectively) than Devinant et al. (2002) and Kamada et al. (2011) ($x/M = 5$ and 6.6, respectively). The stall angle behaviour in the present study agrees with Wang et al. (2014) and Maldonado et al. (2015) in that it remains constant, and the common feature is that all three studies were sufficiently far from the grids, suggesting a grid-based dependency of the other two studies. We would like to note that this is not conclusive evidence that flow homogeneity is the most significant factor in the stall angle behaviour, as other factors exist, such as the different airfoil profiles.

The lift slopes in the linear range for all cases are shown in Fig. 8. The first two cases, FST1.1 and FST 1.6, show lower lift slopes than REF, while all other cases with greater T_i show higher values. It would appear that T_i between 1% and 2% causes a reduction in lift in the linear range, while T_i greater than 2% increases lift. These trends are more prominently shown in Fig. 9, where the relative difference of C_l compared to REF is plotted. There is a clear division into two distinct groups based on T_i. FST1.1 and FST1.6 show consistently lower C_l in the linear region than

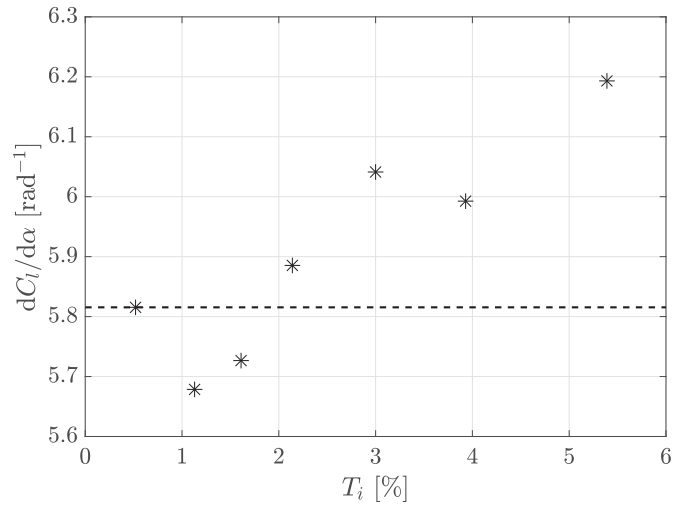

Fig. 8. C_l slope in the linear region for all test cases; the dotted line denotes the lift slope of REF.

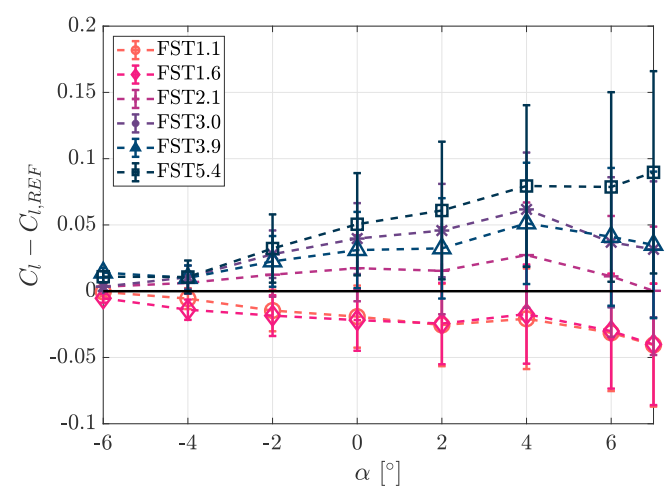

Fig. 9. C_l differences in the linear region for all test cases compared to REF.

REF while all the other cases show higher C_l. It should be noted that the differences shown by FST1.1 and FST1.6 in C_l are near the limit of the estimated uncertainties in the measurements. Nevertheless, the C_l for these two cases in the linear region are consistently lower than that of REF, suggesting the observed trend is real. Upon further examination of the C_p distributions, it was found that this decrease in C_l for FST1.1 and FST1.6 is caused by a reduction in the suction peak region. An example at $\alpha = 7°$ is shown in Fig. 10. The differences in C_p is the greatest at the suction peak.

The overall effect of increasing the FST is an increase in $C_{l,\max}$ and a general increase in the lift slope within the linear region. However, for relatively low T_i (between 1% and 2%), both the lift slope and the absolute C_l values are lower than those for REF in the linear region. This is caused by a reduction in the suction peak of the C_p distributions. In the next section, analysis of the magnitude and frequency content of the fluctuating pressure time-series gives additional insight into the dependence of the pressure and lift characteristics of the airfoil on FST.

4. Time-series analysis of the pressure and lift

While several studies (e.g., those listed in Table 1) have investigated the mean aerodynamic properties for airfoils in FST, as discussed in the previous section, very few explore the time-series information. The RMS

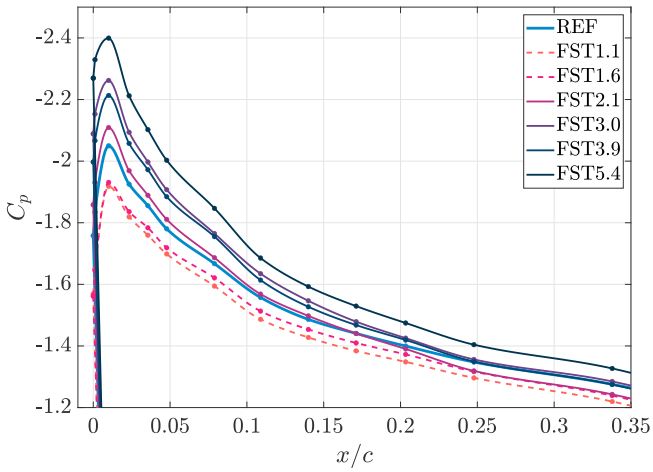

Fig. 10. C_p for $\alpha = 7^\circ$ for all cases, focusing on the suction peak region.

of the suction side pressure fluctuations, p', is calculated for each pressure port for all angles of attack. The results are plotted as contours in Fig. 11, which are normalized by the maximum pressure fluctuations $p'_{\max}$ when $\alpha = 16^\circ$ for each case. The locations of laminar separation bubbles (LSBs) are superimposed unto the contours. Laminar separation bubbles are regions of recirculating flow, and their presence can be detected through the time-averaged C_p distributions. Separation is marked by the start of a pressure "plateau" on the suction side, laminar-turbulent transition marked by the end of the plateau, and reattachment marked by the return to "normal" pressure recovery on the suction side (Gaster, 1967). Example C_p distributions are shown in Fig. 12 along with the identification of the separation (S), transition (T), and reattachment (R) points. A grey dotted line is added to $\alpha = 2^\circ$ in Fig. 12 in order to highlight the signature that LSBs leave on the C_p distribution. The grey line qualitatively represents the C_p distribution if the bubble were not present. The separation point is marked by where the C_p starts to deviate from the grey line, showing a slower pressure recovery; the transition point is marked by a sudden increase in pressure recovery; and the reattachment point is marked by where the C_p returns to the grey line. Due to the relatively high Reynolds number of the present study, the C_p signature of the LSBs, if present, is not always well-defined, as can be seen in the lack of an identifiable separation point for $\alpha = 7^\circ$ for REF in Fig. 12. Therefore, Fig. 11 only shows the separation, transition, and reattachment points of the LSBs that are clearly identifiable from the C_p distributions. The flow separation points associated with near- and post-stall conditions are also included, as marked by the start of a region of constant pressure near $x/c = 0.3$ for $\alpha = 18^\circ$ for REF in Fig. 12. At $\alpha = 18^\circ$, there is a delay in the separation point for cases where $T_i > 2\%$ (FST2.1, FST 3.0, FST3.9, and FST5.4). Furthermore, in these cases, the pressure fluctuations at the leading edge are significantly higher at $\alpha = 18^\circ$ than all the other α. For REF, FST1.1, and FST1.6, this was not observed. The relatively large leading edge pressure fluctuations suggest that the boundary layer is highly energetic at the leading edge, and that the more energetic boundary layer delays flow separation on the suction side of the airfoil at $\alpha = 18^\circ$. This is consistent with the observed higher C_l values at this α for these cases, as well as the delayed separation point extracted from the C_p distributions.

Another observation is that in REF, FST1.1, and FST1.6, the chordwise location of the maximum C_p fluctuations moves upstream with increasing α. This manifests as a series of peaks in Fig. 11 that propagate upstream with increasing α. The peak locations correspond to the transition-reattachment regions found through the C_p distribution, as can be seen in the superimposed points. This suggests that the peaks in the pressure fluctuations on the suction side are associated with the transition and reattachment process in the LSBs. For the other cases, the peaks decrease in prominence, which is reflected in the decreasingly identifiable separation and reattachment points in the C_p distributions. Examining the bubble regions in Fig. 11, it can be observed that for α between 0° and 7°, the bubbles form between $0.5 < x/c < 0.8$. Additionally, small separation bubbles near the leading edge can be observed for α between 9° and 13°. Like the larger bubbles at lower α, these small bubbles also leave decreasingly identifiable signatures on the C_p distributions as T_i increases. Furthermore, for α between 0° and 7°, the relative pressure fluctuations at the leading edge is significantly higher for cases where T_i is greater than 2%. As the pressure fluctuations are normalized by the maximum fluctuations, which occurs near the leading edge, it shows that as T_i increases, the relative intensity of the leading edge pressure fluctuations increase. The observed effect of this is a reduction in the relative pressure fluctuation intensities associated with the separation bubbles. This suggests that the effect of laminar separation bubbles, if present, on the surface pressure fluctuations decrease with increasing T_i.

The increase in leading edge pressure fluctuations can be better observed in Fig. 13, which shows the normalized differences in the suction side pressure fluctuations with respect to REF. For FST1.1 and FST1.6, the differences near the leading edge are not significantly different from the rest of the suction side. However, starting from FST2.1, the leading edge pressure fluctuation differences become much higher than the rest of the suction side, and the region where this difference is prominent expands with increasing T_i. In addition, the pressure fluctuation differences at the highest α for FST2.1 to FST5.4 are significantly higher than that of the other α. This reflects the earlier observation of high levels of pressure fluctuations for these cases at this α, and of delays in flow separation that results in higher C_l in this post-stall region. It is also interesting to note that when REF is subtracted from the other cases, the series of peaks in the pressure fluctuations observed in REF in Fig. 11 leaves its trace in all the difference contours in Fig. 13. The trace manifests itself as a series of negative peaks in the contours, revealing that the pressure fluctuations associated with bubble transition and reattachment in REF are higher than those in the other cases. It is also evident that as FST increases, the pressure fluctuations along this trace decrease, reflected through the increasingly negative values seen in the peaks. This further suggests that as FST increases, the effect of laminar separation bubbles on the flow over the suction side decreases, and it is instead increasingly dominated by the more energetic boundary layer at the leading edge.

Fig. 14 examines the frequency content of the suction side pressure fluctuations at $\alpha = 4^\circ$, 12°, and 18°, representing the linear, near-stall, and post-stall regimes. Localized peaks near normalized frequencies $fc/U_\infty = 0.1$ and 0.2 are observed for nearly all conditions shown. These peaks also extend over the entire suction side surface. These peaks are most prominent for FST1.1 and FST1.6, where we also see a cluster of secondary peaks near $fc/U_\infty = 1$ over the entire surface for $\alpha = 4^\circ$. This secondary cluster is reduced in prominence for cases with higher FST, and is more restricted to the aft portion of the airfoil, as opposed to the entire surface for FST1.1 and FST1.6. In fact, as FST increases, more and more of the airfoil suction side exhibits more energetic pressure fluctuations across a broad bandwidth than the energy contained in this cluster of secondary peaks near $fc/U_\infty = 1$. Similar behaviour is observed for $\alpha = 12^\circ$, except at this angle, the front portion of the airfoil for FST1.1 and FST1.6 exhibits stronger pressure fluctuations across a broad bandwidth, similar to the behaviour seen for higher FST cases. It is postulated that these secondary surface pressure fluctuations are causing flow instabilities on the suction side, which in turn leads to a reduction in the time-averaged lift produced by the airfoil. The increased FST in the other flow cases is believed to have influenced the flow on the suction side sufficiently such that the pressure fluctuations at $fc/U_\infty = 1$ are suppressed, so that they do not have an adverse impact on the overall lift performance of the airfoil. While we do not make the claim here that vortex shedding is present in the airfoil's wake under the tested flow conditions, it is possible that these pressure fluctuations are traces left by potential velocity fluctuations in the flow around the airfoil, and that the

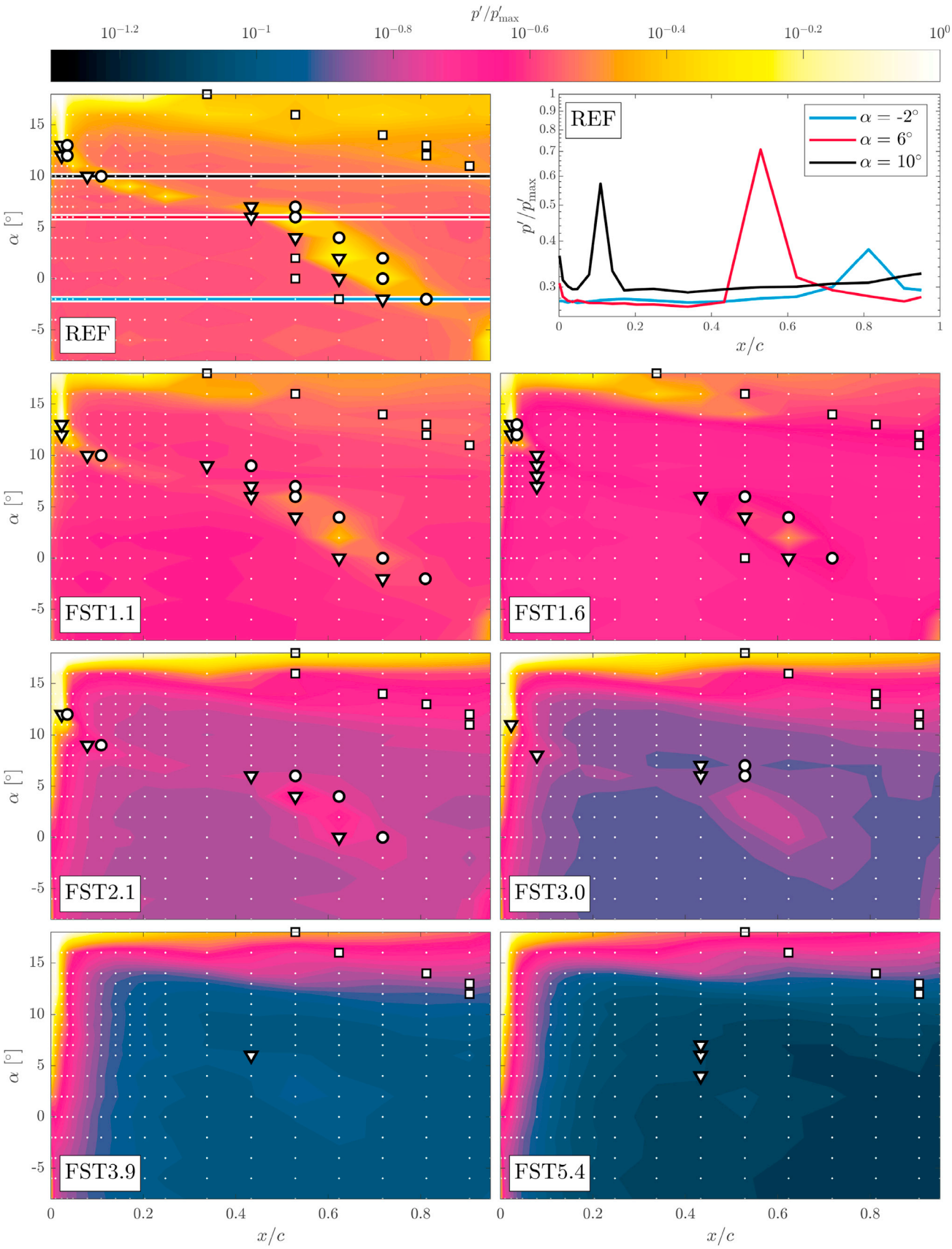

Fig. 11. Normalized suction side pressure fluctuations. Example 2-D pressure fluctuations are also plotted for REF for selected α, highlighting the progression of the fluctuation peak as α increases; the corresponding αs are noted in the contour for REF as horizontal lines. The transition and reattachment points estimated from the C_p distributions are superimposed; (▽) denotes transition, (◦) denotes reattachment, and (□) denotes separation. When no symbols are present for a given α, it implies that these points cannot be distinctly identified through the C_p distributions. The white dots identify measurement points.

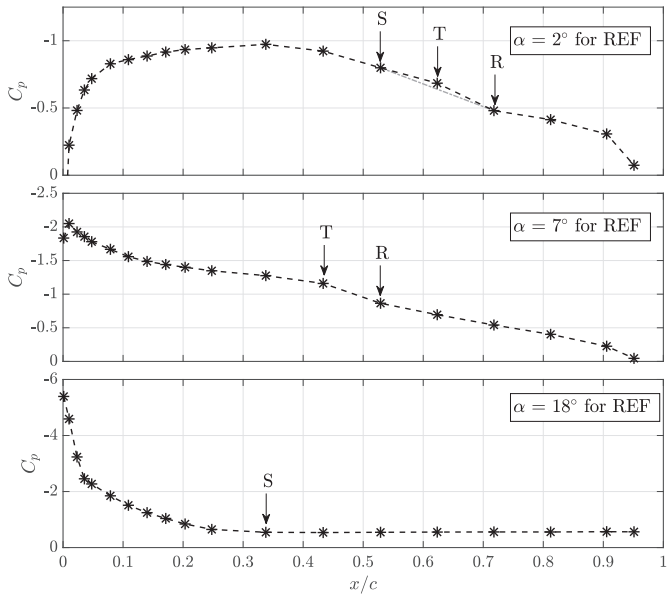

Fig. 12. Example suction side C_p distributions for demonstrating the identification of separation (S), transition (T), and reattachment (R) points for LSBs and near- and post-stall flow separation. A grey dotted line is added to the C_p distribution for $\alpha = 2^\circ$ to highlight the C_p signature of a LSB.

elevated T_i has a suppression effect on them. Interestingly, this cluster of secondary peaks appears to be the least prominent in REF, where FST is the lowest. This suggests that T_i between 1% and 2% excites these fluctuations, leading to their noticeable presence in FST1.1 and FST1.6. Taniguchi et al. (2012) found that low FST (<4%) causes noticeable velocity fluctuations to develop in the shear layer of LSBs through Kelvin-Helmholtz instabilities on a low pressure turbine blade. At higher T_i, bypass transition occurs in the airfoil boundary layer, leading to an overall diminished effect of the LSBs on the flow field. Similar observations have been made by Istvan and Yarusevych (2018) for a NACA0018 airfoil. Fransson et al. (2005) found that in a boundary layer on a flat plate, the initial disturbance energy $E = u'^2/U^2$ scales with T_i^2, which implies that a small increment in T_i can lead to a large increase in the initial disturbance energy in the boundary layer, leading to an earlier onset of bypass transition. It is possible that in the present study, when the FST is relatively low (between 1% and 2%), it amplified the velocity fluctuations in the LSB shear layer while not being strong enough to induce an early onset of bypass transition in the boundary layer. These velocity fluctuations then leave their signature in the surface pressure fluctuations as peaks near $fc/U_\infty = 1$. As T_i increases, it becomes strong enough to induce an early onset of bypass transition, thus diminishing the overall effect of the LSBs, leading to a suppression of these peaks. This earlier onset of bypass transition in the boundary layer can potentially be reflected by the leading edge pressure exhibiting increasingly energetic fluctuations across a broad bandwidth, starting from FST2.1. This is consistent with the observation of increased pressure fluctuations at the leading edge as FST increases. It is also interesting to note that for REF, FST1.1, and FST1.6 at $\alpha = 18^\circ$, the front portion of the airfoil experiences high energy pressure fluctuations at relatively low frequencies ($fc/U_\infty < 0.1$), while the aft portion of the airfoil does not. This can be seen in Fig. 14 as two groupings of the spectra for $fc/U_\infty < 0.1$, for REF, FST1.1, and FST1.6 at $\alpha = 18^\circ$. The split in the grouping occurs near $x/c = 0.3$, which is where flow separation occurs as identified from the C_p distributions. For all the other cases, the pressure fluctuations extend across most of the airfoil and include higher frequency content. The change is also gradual as opposed to the abrupt change seen in REF, FST1.1, and FST1.6. This observation further suggests that the increased T_i beyond 2% is able to energize the boundary layer sufficiently to delay flow separation in the post-stall region. Lastly, the increase in energy associated with the pressure fluctuation peaks caused by laminar separation bubbles can be seen in Fig. 14 as elevated spectra in comparison to their neighbours. The increase in energy is broadband, suggesting that the transition and reattachment mechanisms do not influence the airfoil surface pressure within that region at distinct frequencies.

Fig. 15 shows the spectrogram of the computed C_l time-series for all cases. In FST1.1 and FST1.6, traces of the pressure spectral peaks near $fc/U_\infty = 0.2$ and 1 are evident in the spectra for C_l. The peak at $fc/U_\infty = 0.2$ is less prominent in REF, and all localized peaks are suppressed in the other flow cases with higher FST. The main difference in the C_l spectrograms between REF, FST1.1, and FST1.6 is the presence of the peaks near $fc/U_\infty = 1$ for the latter cases. It suggests the possible presence of LSB shear layer velocity fluctuations as observed by Taniguchi et al. (2012), and that these fluctuations are amplified by the relatively low T_i. As the FST increases, the high energy pressure fluctuations observed near the leading edge dominate the frequency space behaviour of C_l.

Finally, the partial variance of C_l is calculated by integrating the PSD from $f = 20$ Hz–40 Hz, as the secondary peaks near $fc/U_\infty = 1$ correspond to $f \approx 30$ Hz. This is done to examine the fraction of the fluctuations contained near the secondary peaks. The results are shown in Fig. 16, normalized by the total C_l variance. From $\alpha = 5^\circ$–14°, FST1.1 and FST1.6 show the highest fraction in terms of energy contained in the fluctuations near $fc/U_\infty = 1$, while REF shows the lowest. This is consistent with the results shown in the C_l spectrogram, as well as the pressure fluctuation PSDs, in that FST1.1 and FST1.6 show the most prominent peaks near $fc/U_\infty = 1$, and that their C_l are most affected by them. In order to reduce data clutter, only REF, FST1.1, FST1.6 and FST3.9 are shown in Fig. 16, but these cases are representative.

The analyses of the pressure and computed C_l time-series suggest that areas of high pressure fluctuations are associated with the transition and reattachment mechanisms of LSBs. Pressure fluctuations at certain localized frequencies are seen for FST1.1 and FST1.6, and to a lesser extent for REF. They can be potentially related to vortex shedding in the LSB shear layer as observed by Taniguchi et al. (2012). Higher levels of T_i diminish the overall effects of these pressure fluctuations on C_l, possibly through inducing an earlier onset of bypass transition in the boundary layer, as was observed by Istvan and Yarusevych (2018). This has the effect of reducing the influence of LSBs on the airfoil. Indeed the appearance of these localized peaks in the C_l spectrogram for FST1.1 and FST1.6 suggests that these fluctuations are possibly causing flow instabilities to develop over the suction side. This is a possible cause for the reduction of the suction peak in the time-averaged C_p, with the overall effect being a reduction in the time-averaged lift produced by the airfoil.

5. Conclusions

In the present study, a reference wind turbine airfoil was subjected to seven different incoming flows with varying turbulence intensities. It was found that an increase in T_i caused a general increase in the maximum lift coefficient, which is consistent with past investigations into other airfoils. The lift slope was also found to increase with increasing T_i. This contrasts with the findings from some previous studies, but this is suspected to be caused by differences in the homogeneity of the incoming flow. Wang et al. (2014) and Maldonado et al. (2015) reported lift slopes that were either unchanged or increased with increasing T_i; both studies had strong flow homogeneity at a position well downstream of the turbulence generation, similar to the present investigation. We do not make the claim that flow homogeneity is the most significant factor at play, but it certainly would have an effect. A rigorous investigation of the impact of homogeneity would be insightful, but is out of the scope of the present investigation. The stall angle was not found to be strongly influenced by FST. Through the analysis of C_p distributions and integrated lift curves, it was observed that within the linear operational region of the airfoil, T_i between 1% and 2% caused a reduction in the pressure suction peak compared to the reference quasi-laminar case (REF), and as a consequence, the C_l values decreased. This may be of interest to the field

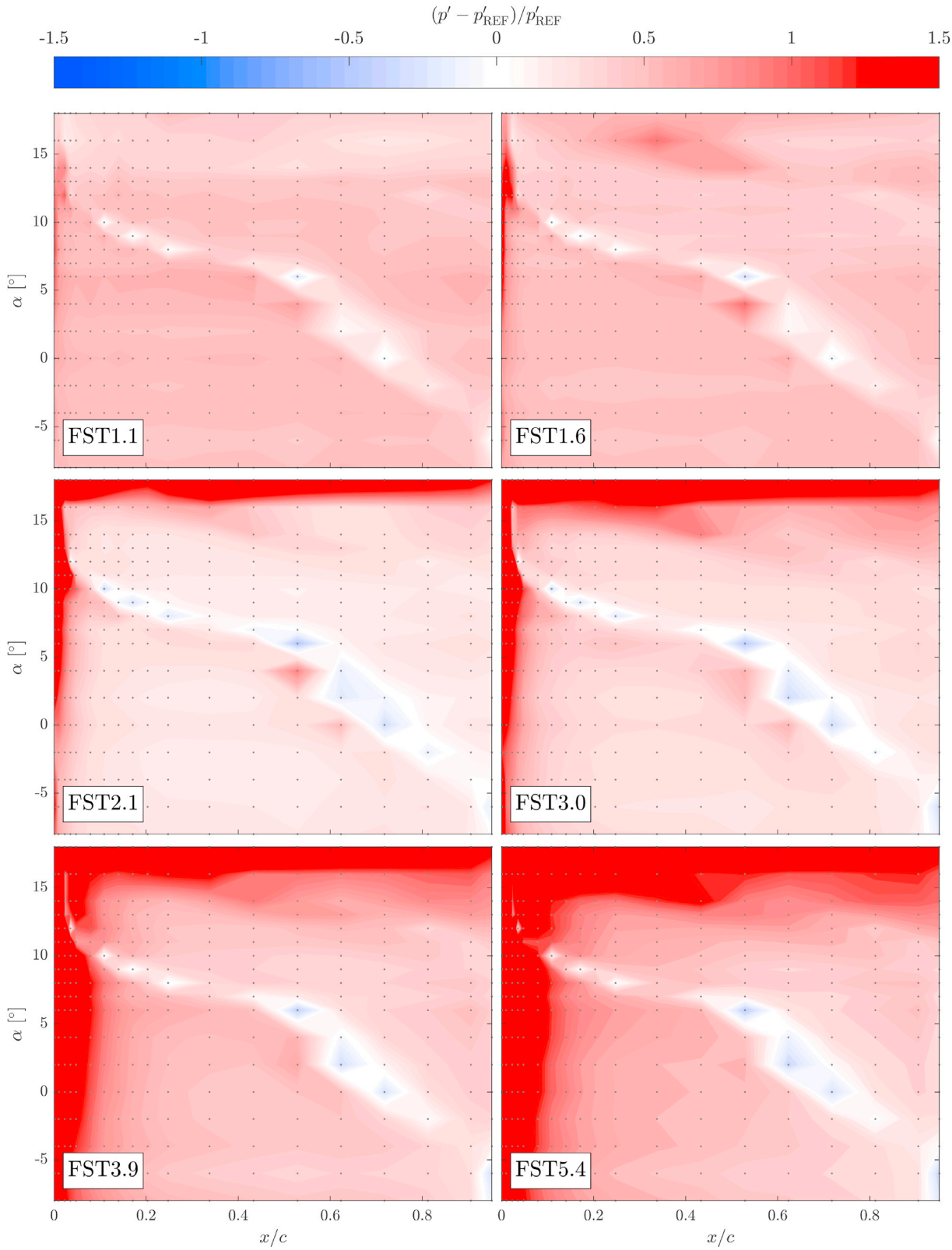

Fig. 13. Normalized suction side pressure fluctuation difference. The grey dots identify measurement points.

application of this airfoil, as it is designed to be used at the tips of rotor blades, and consequently would experience atmospheric turbulence intensities of similar level when TSR is taken into account. At higher values of T_i, the pressure suction peak increased with respect to REF, resulting in both higher absolute values of C_l and C_l slope. Examinations of the frequency content of the surface pressure signals revealed the presence of localized peaks at $fc/U_\infty = 0.2$ and 1 for these low FST cases. It is postulated that T_i between 1% and 2% excites these periodic oscillations, which in turn causes flow instabilities on the suction side of the airfoil. The overall effect is a reduction in the time-averaged lift. Higher T_i

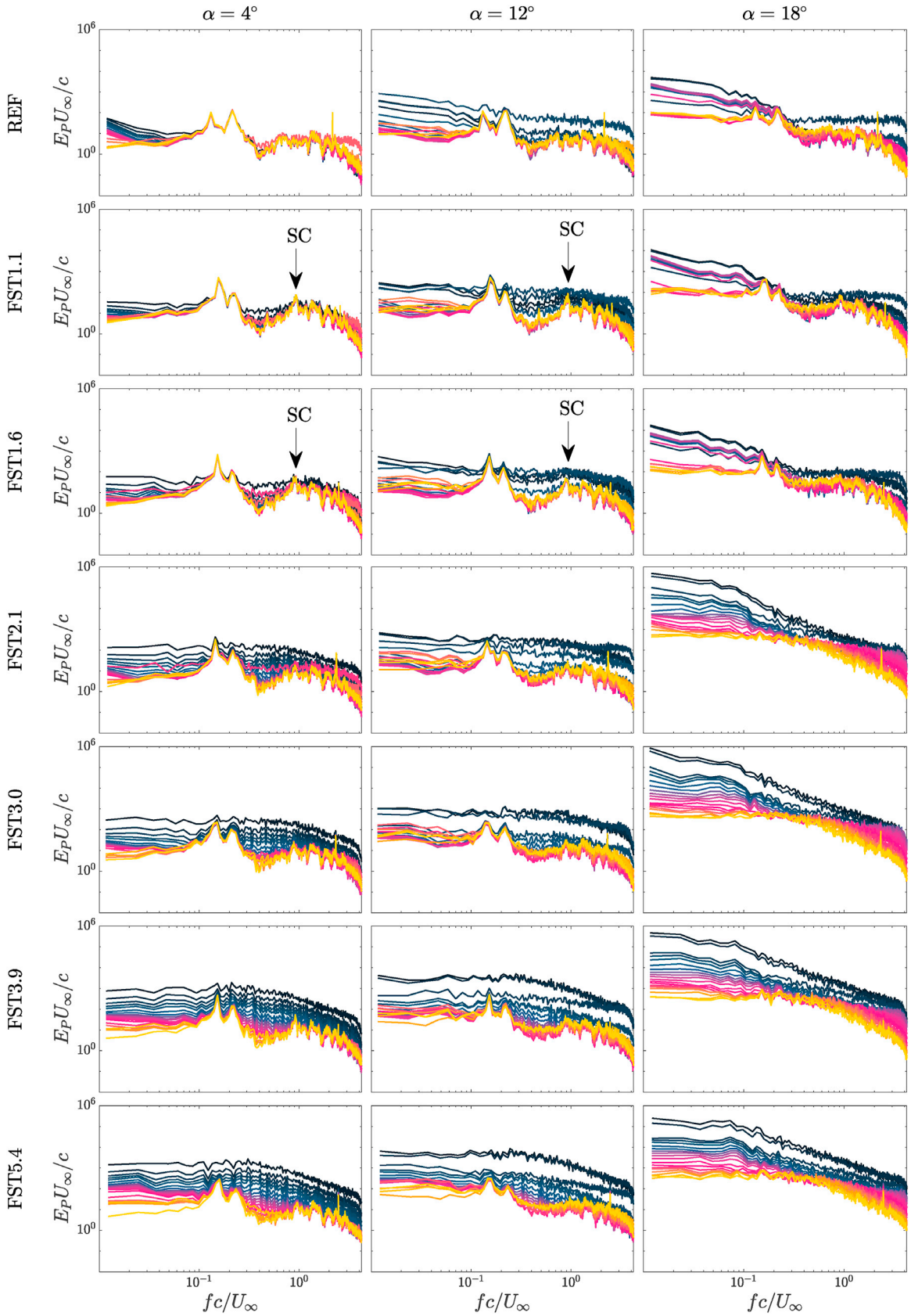

Fig. 14. Normalized suction side pressure fluctuation power spectral density for all flow cases at selected α. The light to dark colours denote pressure port positions from the trailing edge to the leading edge; prominent occurrences of the secondary cluster are marked with an arrow and "SC". (For interpretation of the references to colour in this figure legend, the reader is referred to the Web version of this article.)

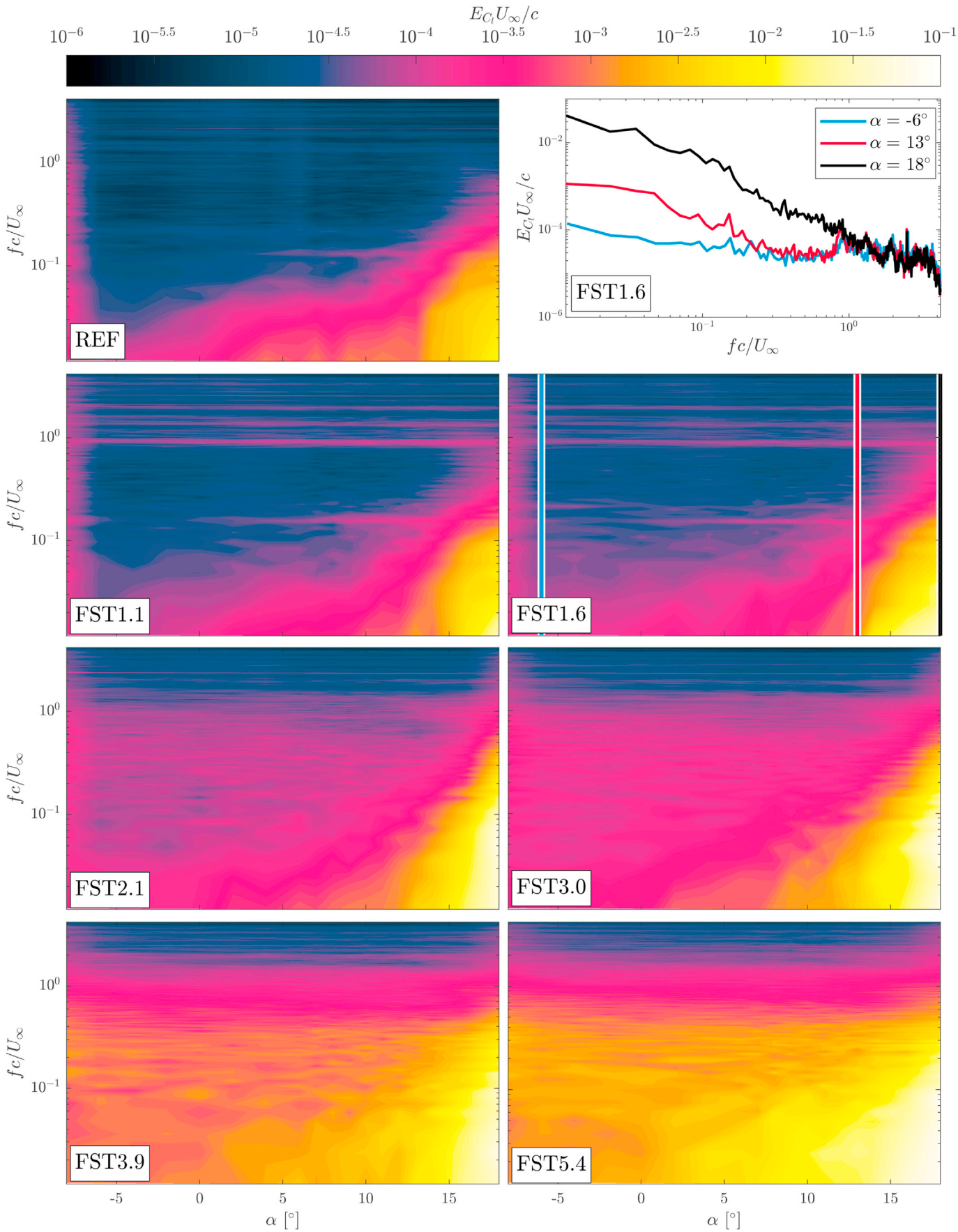

Fig. 15. Normalized spectrogram of the lift coefficient power spectral density for all flow cases. Example 2-D PSDs are plotted for FST1.6 to highlight the local peaks near $fc/U_\infty = 1$. The αs shown in the example plot are highlighted in the spectrogram for FST1.6 as vertical lines.

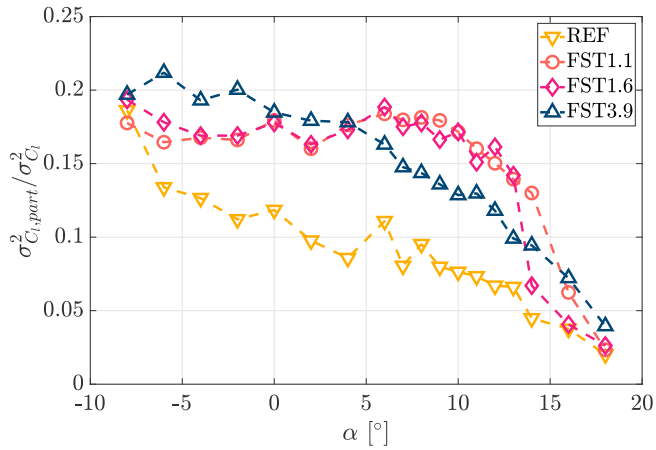

Fig. 16. Partial variance of C_l calculated by integrating the C_l PSD from $f = 20$ Hz–40 Hz, normalized by the total variance. Only REF, FST1.1, FST1.6, and FST3.9 are shown to reduce clutter; the behaviour of FST3.9 is representative of the other omitted cases.

suppressed these peaks, leading to an increase in lift produced by the airfoil. In the post-stall regime, elevated FST delayed flow separation and increased lift.

The present work investigated seven different flow cases, which is more than previous studies of a similar nature. It also combined time-averaged pressure and lift characteristics with the spectral analysis of their frequency content to offer further insight into the underlying physics. Lastly, the turbulence intensities as well as the Reynolds number investigated here are representative of the field application of this airfoil, thus the results presented herein provide valuable performance and validation data for future uses and studies of this airfoil.

Division of work

LL and RJH conceived of the idea for this work. LL conducted the experiments, performed the analysis, and was the primary author of the manuscript with support from RJH. RJH supervised the project. All authors read and contributed to the manuscript.

CRediT authorship contribution statement

Leon Li: Methodology, Software, Formal analysis, Investigation, Writing - original draft, Visualization. **R. Jason Hearst:** Conceptualization, Methodology, Resources, Writing - review & editing, Supervision, Project administration, Funding acquisition.

Declaration of competing interest

The authors declare that they have no known competing financial interests or personal relationships that could have appeared to influence the work reported in this paper.

Acknowledgement

We would like to thank Magnus K. Vinnes and Håkon T. Nygård for their help in setting up and running parts of the experiment. We would also like to thank Professor Ole Øiseth from the Department of Structural Engineering at NTNU for lending us the pressure scanner for the airfoil measurements.

References

Barlow, J.B., Rae, W.H., Pope, A., 1999. Low-speed Wind Tunnel Testing, third ed.Ch. 9. John wiley & sons, pp. 352–355.
Bartl, J., Sagmo, K.F., Bracchi, T., Sætran, L., 2019. Performance of the NREL S826 airfoil at low to moderate Reynolds numbers - a reference experiment for CFD models. Eur. J. Mech. B Fluid 75, 180–192.
Benedict, L., Gould, R., 1996. Towards better uncertainty estimates for turbulence statistics. Exp. Fluid 22 (2), 129–136.
Bianchi, F.D., Mantz, R.J., Battista, H.D., 2007. The Wind and Wind Turbines. Springer.
Blackburn, H.M., Melbourne, W.H., 1996. The effect of free-stream turbulence on sectional lift forces on a circular cylinder. J. Fluid Mech. 306, 267–292.
Butler, R.J., Byerley, A.R., VanTreuren, K., Baughn, J.W., apr 2001. The effect of turbulence intensity and length scale on low-pressure turbine blade aerodynamics. Int. J. Heat Fluid Flow 22 (2), 123–133.
Cao, N., Ting, D.S.-K., Carriveau, R., 2011. The performance of a high-lift airfoil in turbulent wind. Wind Eng. 35 (2), 179–196.
Comte-Bellot, G., Corrsin, S., 1966. The use of a contraction to improve the isotropy of grid-generated turbulence. J. Fluid Mech. 25, 657–682.
Devinant, P., Laverne, T., Hureau, J., jun, 2002. Experimental study of wind-turbine airfoil aerodynamics in high turbulence. J. Wind Eng. Ind. Aerod. 90 (6), 689–707.
Ertunç, O., Özyilmaz, N., Lienhart, H., Durst, F., Beronov, K., 2010. Homogeneity of turbulence generated by static-grid structures. J. Fluid Mech. 654, 473–500.
Fransson, J.H., Matsubara, M., Alfredsson, P.H., 2005. Transition induced by free-stream turbulence. J. Fluid Mech. 527, 1–25.
Gaster, M., 1967. The Structure and Behaviour of Laminar Separation Bubbles. NPL.
Hann, R., Hearst, R.J., Sætran, L.R., Bracchi, T., 2020. Experimental and numerical icing penalties of an S826 airfoil at low Reynolds numbers. Aerospace 7 (4), 46.
Hearst, R.J., Lavoie, P., 2014. Decay of turbulence generated by a square-fractal-element grid. J. Fluid Mech. 741, 567–584.
Hoffmann, J.A., 1991. Effects of freestream turbulence on the performance characteristisc of an airfoil. AIAA J. 29 (9), 1353–1354.
Huang, R.F., Lee, H.W., 1999. Effects of freestream turbulence on wing-surface flow and aerodynamic performance. J. Aircraft 36 (6), 965–972.
Isaza, J., Salazar, R., Warhaft, Z., 2014. On grid-generated turbulence in the near- and far field regions. J. Fluid Mech. 753, 402–426.
Istvan, M.S., Yarusevych, S., 2018. Effects of free-stream turbulence intensity on transition in a laminar separation bubble formed over an airfoil. Exp. Fluid 59 (3), 52.
Kamada, Y., Maeda, T., Murata, J., Toki, T., Tobuchi, A., 2011. Effects of turbulence intensity on dynamic characterstics of wind turbine airfoil. J. Fluid Sci. Technol. 6 (3), 333–341.
Larssen, J.V., Devenport, W.J., 2011. On the generation of large-scale homogenous turbulence. Exp. Fluid 50, 1207–1223.
Li, Q.A., Kamada, Y., Maeda, T., Murata, J., Nishida, Y., 2016. Effect of turbulent inflows on airfoil performance for a Horizontal Axis Wind Turbine at low Reynolds numbers (Part I: static pressure measurement). Energy 111, 701–712.
Maldonado, V., Castillo, L., Thormann, A., Meneveau, C., 2015. The role of free stream turbulence with large integral scale on the aerodynamic performance of an experimental low Reynolds number S809 wind turbine blade. J. Wind Eng. Ind. Aerod. 142, 246–257.
Michálek, J., Monaldi, M., Arts, T., 2012. Aerodynamic performance of a very high lift low pressure turbine airfoil (T106C) at low Reynolds and high mach number with effect of free stream turbulence intensity. J. Turbomach. 134.
Mücke, T., Kleinhans, D., Peinke, J., Feb 2011. Atmospheric turbulence and its influence on the alternating loads on wind turbines. Wind Energy 14 (2), 301–316.
Mueller, T.J., Pohlen, L.J., Conigliaro, P.E., Jansen, B.J., 1983. The influence of free-stream disturbances on low Reynolds number airfoil experiments. Exp. Fluid 1 (1), 3–14.
Owen, P.R., Klanfer, L., 1953. On the Laminar Boundary Layer Separation from the Leading Edge of a Thin Aerofoil. Tech. Rep.. AERONAUTICAL RESEARCH COUNCIL LONDON (UNITED KINGDOM).
Ravi, S., Watkins, S., Watmuff, J., Massey, K., Petersen, P., Marino, M., 2012a. Influence of large-scale freestream turbulence on the performance of a thin airfoil. AIAA J. 50 (11).
Ravi, S., Watkins, S., Watmuff, J., Massey, K., Petersen, P., Marino, M., Ravi, A., 2012b. The flow over a thin airfoil subjected to elevated levels of freestream turbulence at low Reynolds numbers. Exp. Fluid 53, 637–653.
Sarlak, H., Frère, A., Mikkelsen, R., Sørensen, J.N., 2018. Experimental investigation of static stall hysteresis and 3-dimensional flow structures for an NREL S826 wing section of finite span. Energies 11 (6).
Sarlak, H., Mikkelsen, R., Sarmast, S., Sørensen, J.N., 2014. Aerodynamic behaviour of NREL S826 airfoil at Re= 100,000. In: J. Physics: Conference Series, vol. 524. IOP Publishing, 012027.
Sarlak Chivaee, H., Sørensen, J.N., 2018. Characterisation of mushroom structures on airfoils: CFD and wind tunnel investigation. In: 21st Australasian Fluid Mechanics Conference.
Sarmast, S., Mikkelsen, R.F., 2012. The Experimental Results of the NREL S826 Airfoil at Low Reynolds Numbers.
Schneemann, J., Knebel, P., Milan, P., Peinke, J., 2010. Lift measurements in unsteady flow conditions. In: DEWEK 2010.
Sicot, C., Aubrun, S., Loyer, S., Devinant, P., 2006. Unstead characteristics of the static stall of an airfoil subjected to freestream turbulence level up to 16%. Exp. Fluid 41, 641–648.
Somers, D.M., 2005. The S825 and S826 Airfoils. Tech. rep., SR-500-36344, NREL. https://wind.nrel.gov/airfoils/Documents/S825,S826_Design.pdf.
Stack, J., 1931. Test in the variable density wind tunnel to investigate the effects of scale and turbulence on airfoil characteristics. Tech. Rep. 364. NACA.
Swalwell, K.E., Sheridan, J., Melbourne, W.H., 2001. The effect of turbulence intensity on stall of the NACA 0021 aerofoil. In: 14th Australasian Fluids Mechanics Conference.

Taniguchi, H., Sakai, H., Funazaki, K.-i., 2012. Effects of freestream turbulence on bypass transition of separated boundary layer on low-pressure turbine airfoils. J. Therm. Sci. 21 (3), 230–235.
Wang, S., Zhou, Y., Alam, M.M., Yang, H., 2014. Turbulence intensity and Reynolds number effects on an airfoil at low Reynolds number. Phys. Fluids 26 (115107).
Watkins, S., Ravi, S., Loxton, B., 2010. The effect of turbulence on the aerodynamics of low Reynolds number wings. Eng. Lett. 18 (3).
West, G.S., Apelt, C.J., 1982. The effects of tunnel blockage and aspect ratio on the mean flow past a circular cylinder with Reynolds numbers between 10^4 and 10^5. J. Fluid Mech. 114, 361–377.
Yalçın, Ö., Cengiz, K., Özyörük, Y., 2018. High-order detached eddy simulation of unsteady flow around NREL S826 airfoil. J. Wind Eng. Ind. Aerod. 179, 125–134.